DPC Direct Disposal Postclosure Thermal Modeling

Spent Fuel and Waste Disposition

Prepared for
US Department of Energy
Spent Fuel and Waste Science and Technology
Kyung Won Chang and Philip Jones

August 31, 2022
SAND2022-XXXX
M4SF-22SN010305114

This is a technical report that does not take into account the contractual limitations under the Standard Contract for Disposal of Spent Nuclear Fuel and/or High-Level Radioactive Waste (Standard Contract) (10 CFR Part 961). For example, under the provisions of the Standard Contract, DOE does not consider spent nuclear fuel in multi-assembly canisters to be an acceptable waste form, absent a mutually agreed to contract amendment. To the extent discussions or recommendations in this report conflict with the provisions of the Standard Contract, the Standard Contract governs the obligations of the parties, and this report in no manner supersedes, overrides, or amends the Standard Contract. This report reflects technical work which could support future decision making by DOE. No inferences should be drawn from this paper regarding future actions by DOE, which are limited both by the terms of the Standard Contract and a lack of Congressional appropriations for the Department to fulfill its obligations under the Nuclear Waste Policy Act including licensing and construction of a spent nuclear fuel repository.

Prepared by
Sandia National Laboratories
Albuquerque, New Mexico 87185

Sandia National Laboratories is a multimission laboratory managed and operated by National Technology & Engineering Solutions of Sandia, LLC, a wholly owned subsidiary of Honeywell International Inc., for the U.S. Department of Energy's National Nuclear Security Administration under contract DE-NA0003525.
SAND2022-XXXX X.

SUMMARY

Performance of geologic radioactive waste repositories depends on near-field and far-field processes, including km-scale flow and transport in engineered and natural barriers, that may require simulations of up to 1 M years of regulatory period. For a relatively short time span (less than 1000 years), the thermo-hydro-mechanical-chemical (THMC) coupled processes caused by heat from the waste package will influence near-field multiphase flow, chemical/reactive transport, and mechanical behaviors in the repository system. This study integrates the heat-driven perturbations in thermo-hydro-mechanical characteristics into thermo-hydro-chemical simulations using PFLOTRAN to reduce dimensionality and improve computational efficiency by implementing functions of stress-dependent permeability and saturation-temperature-dependent thermal conductivity. These process couplings are developed for spent nuclear fuel in dual-purpose canisters in two different hypothetical repositories: a shale repository and a salt repository.

Our reduced-order THMC simulation of a single waste package in a shale-hosted repository reveals three physical mechanisms associated with heat pulse emitted from the waste package: (1) increase of liquid mobility that accelerates the inflow and solute transport from the fully saturated host rock, (2) production of thermal gradients that results in outward flow within the buffer and disturbed rock zone (DRZ) nearest the waste package, and (3) reduction of thermal conductivity that confines heat within the engineered barrier system. These combined hydro-thermal mechanisms influence the rate of re-saturation process and transport/exchange of corrosive species in the repository system.

A finite-difference thermo-mechanical model including the effects of salt creep was implemented in FLAC2D. The model was used to investigate the impact of model parameters on near field temperatures. Because backfill consolidation occurs much sooner than the time to peak near field temperatures in this analysis, the choice of viscoplastic constitutive model has little impact on the temperature evolution. Bounding simulations over the possible ranges of intact and consolidated salt thermal conductivity were conducted and found to change the peak temperatures up to about ± 10 K for the hottest canister investigated. It is increasingly evident that large hot waste packages induce significant hydrologic effects in a potential salt formation. Without taking these effects into account, it is difficult to draw meaningful conclusions pertaining to the temporal temperature evolution. Future analysis would benefit from accounting for coupled thermo-hydro-mechanical effects.

This page is intentionally left blank.

ACKNOWLEDGEMENTS

The authors would like to acknowledge Tara LaForce and Laura Price of Sandia National Laboratories who helped guide this work. Thanks also go to Tim Gunter of the Department of Energy for sponsoring this work. Section 2 was contributed by Kyung Won Chang, and Section 3 by Philip Jones.

This page is intentionally left blank.

CONTENTS

LIST OF FIGURES

LIST OF TABLES

ACRONYMS

DPC	dual-purpose canister
DRZ	disturbed rock zone
FY	fiscal year
ISFSI	independent spent fuel storage installation
MPC	multi-purpose canister
SNF	spent nuclear fuel
THMC	thermo-hydro-mechanical-chemical
TPHM	Two-Part Hooke's Model
UNF-ST&DARDS	Used Nuclear Fuel – Storage, Transportation & Disposal Analysis Resource and Data Systems
WIPP	Waste Isolation Pilot Plant
WP	waste package

This page is intentionally left blank.

SPENT FUEL AND WASTE SCIENCE AND TECHNOLOGY

DPC DIRECT DISPOSAL POSTCLOSURE THERMAL MODELING

1. INTRODUCTION

This report describes modeling of the thermal effects of disposing of spent nuclear fuel (SNF) in dual-purpose canisters (DPCs) in two different hypothetical repositories: a shale repository and a salt repository. Section 2 presents a hydro-thermal analysis of near-field thermal behaviors in shale while Section 3 presents a thermo-mechanical analysis of thermal behavior in salt.

This report represents completion of Milestone M4SF-22SN010305114.

This page is intentionally left blank.

2. HYDRO-THERMAL ANALYSIS OF NEAR-FIELD BEHAVIORS IN SHALE

This section describes a multiphysics-coupled modeling approach to model the effects of heat on the near-field behavior of the materials in a hypothetical shale repository used to dispose of SNF in DPCs. This study implements the PFLOTRAN code, a three-dimensional massively parallel subsurface flow and transport simulator (Lichtner & Hammond (2012)), which has been used for multi-scale and multiphysics performance assessment (PA) simulations of deep geologic repository systems (Sevougian et al., 2019; Mariner et al.,2020, 2021; LaForce et al., 2020, 2021). The immediate motivation for using PFLOTRAN for DPC thermal modeling is to include a mechanistic description of backfill and host rock hydration/dehydration corresponding to a range of DPC thermal histories.

This study simulates hydro-thermal behaviors in the near-field of a shale-hosted repository system. The clay-rich sedimentary strata have been considered a potential medium for disposal of radioactive waste in the United States since the forerunner to the Department of Energy introduced a program to develop radioactive waste disposal technology in 1976 (Shurr (1977), Gonzales & Johnson (1985), Rechard et al. (2011)). Clay-rich formations are an attractive disposal medium due to its desirable characteristics:

- Low permeability
- High sorption capacity, typically reducing pore-waters (which limit radionuclide solubility)
- Plastically deformable, which promotes self-healing of fractures

Note that clay-rich formations suitable for isolation of radioactive waste span a range of rock types, varying in degree of foliation and degree of consolidation and induration, from unconsolidated mud (such as the Boom Clay) to argillite (such as the Callovo-Oxfordian argillite), but the term “shale” is used somewhat imprecisely to represent all kinds of clay-rich rocks in this report.

2.1 Model Setting

2.1.1 Model Domain

The model domain represents a quarter of a waste package in the shale repository system, with the center of the waste package located at a depth of 500 m below the land surface (Figure 2-1A). Three concentric sections of waste package, buffer, and DRZ at 1 m, 2.4 m, and 4.07 m in radius, respectively, are modeled in the 35 m (width) x 10 m (length) x 75 m (height) domain (Figure 2-1B). The buffer dimension is based on the size of a circular drift with a diameter of 4.8 m, and the half-length of a waste package is set at 2.5 m.

Assuming the model domain is a porous medium, the waste package porosity is set equal to the fraction of void space within the section of waste package (50%) in the repository system. The permeability is 1×10^{-16} m^2, several orders of magnitude higher than that of the surrounding materials (Table 2-1), so that flow through the waste package is uninhibited which describes potential water seepage into the waste package. The installed package consists of a stainless-steel canister (the canister) and a stainless steel overpack, and thus, the thermal properties of stainless steel are implemented for the waste package (Shelton (1934)).

Geological heterogeneity, often observed in sedimentary basins (e.g. layered system), has been neglected in this small-scale near-field analysis, such that the 75-m thick layer represents a homogeneous portion of shale host rock, with properties appropriate for a sealing shale. The natural barrier system comprises the shale formation hosting the repository and the DRZ, defined as the portion of the host rock adjacent to the engineered barrier system. Prior to installing waste forms, the localized DRZ experiences durable (but not necessarily permanent) perturbations of hydrological and/or mechanical characteristics of the host rock (e.g. fracture opening) due to excavation for the repository. In the reference model, the initial enhancement of hydraulic diffusivity by excavation-driven fracturing is represented implicitly by assigning one order of magnitude larger permeability to the DRZ than to the undisturbed host rock.

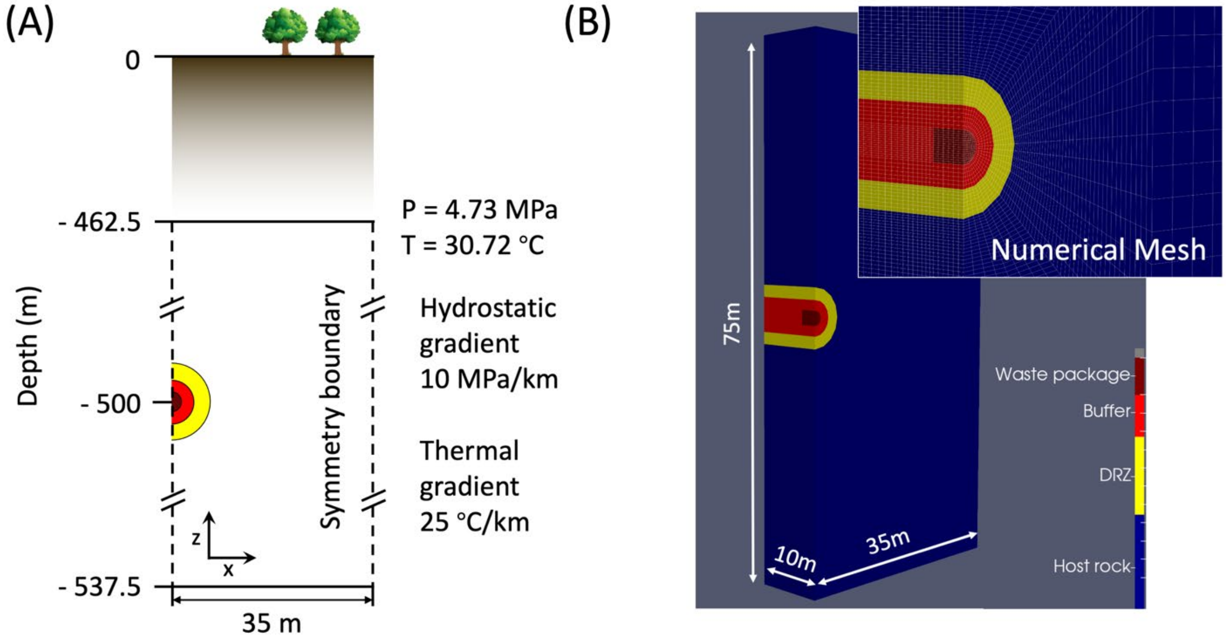

Figure 2-1. Model description and setting. (A) Schematic description (not to scale) of the model domain consisting of waste package (maroon), buffer (red), disturbed rock zone (yellow), and shale host rock (navy). (B) Numerical domain with mesh setting.

The current set of simulations employs a buffer material with properties appropriate for a compacted mixture of 70% bentonite and 30% quartz sand in the buffer. The buffer is assigned a porosity of 0.35 and a permeability of 10^{-20} m^2 (Liu et al. (2016)). The bentonite/sand buffer has a water-saturated thermal conductivity of 1.5 W/m/K and a dry thermal conductivity of 0.6 W/m/K (Jobmann & Buntebarth (2009), Wang et al. (2015)). The material properties of the reference case in which hydrological and thermal parameters of all sections are constant over time are given in Table 2-1.

Initial pressure and temperature throughout the model domain are calculated by applying hydrostatic and geothermal gradients (10 kPa/m and 0.025°C/m, respectively) in the vertical direction assuming a temperature of 19°C and atmospheric pressure at the surface (462.5 m above the top of the model domain). For the unsaturated condition, initial liquid saturation (S_{li}) is set to 0.65 for the buffer and the DRZ, whereas the shale host rock is fully saturated with liquid. Invoking closed symmetry conditions at all side boundaries represents that a waste package is located in the center of an infinite, symmetrical repository system. The simulation runs for 10^3 years.

This near-field model was run in PFLOTRAN's GENERAL mode, which solves two-phase (liquid-gas) miscible flow, coupled to energy for unsaturated conditions in the waste package, buffer, and DRZ. The numerical domain consists of ~5.4×10^4 unstructured grid cells for spatial discretization of the repository system (subset of Figure 2-1B).

Table 2-1. Model parameter values.

Flow and thermal properties			
	Buffer	**DRZ**	**Shale host rock**
Porosity [-]	0.35	0.2	0.2
Permeability [m^2]	1x10^{-20}	1x10^{-18}*	1x10^{-19}
Density [kg/m^3]	2700	2700	2700
Heat capacity [J/(kg-K)]	830	1005	1005
Dry thermal conductivity [W/(K-m)]	0.6	0.6	0.6
Wet thermal conductivity [W/(K-m)]	1.5	1.2	1.2
Initial gas saturation [-]	0.35	0.35	0.0
Residual liquid saturation [-]	0.1	0.1	0.1
Residual gas saturation [-]	0.1	0.1	0.1
Van Genuchten saturation function			
Alpha [1/Pa]	6.25x10^{-8}	6.67x10^{-8}	6.67x10^{-8}
Lambda [-]	0.375	0.333	0.333

*The DRZ permeability will converge to the shale permeability with buffer swelling for comparative models implementing the TPHM permeability function.

2.1.2 Heat Source

Figure 2-2A shows the transient decay heat curves for 10^6 years from three DPCs already loaded with spent nuclear fuel that represent the 10th, 50th, and 75th percentiles of the distribution of heat outputs among a population of 1,981 as-loaded DPCs (Jones et al. (2021)). The three representative DPCs, in ascending percentile order, are the NUHOMS 24PT1 canister installed at the San Onofre Nuclear Independent Spent Fuel Storage Installation (ISFSI) (24PT1-4701D-DSC009), a multi-purpose canister (MPC) installed at the Arkansas ISFSI (MPC-24-MPC-003), and a MPC installed at the Waterford ISFSI (MPC-32-MPC-224), respectively. More details of the procedure generating the heat curve are described in the recent report by Jones et al. (2021).

Thermal energy (watts per waste package volume; 596.92, 1008.38, and 1251.56 W initially for elements representing a quarter of a single waste package) entering the model domain is updated as a function of time according to values in a lookup table. The 50th percentile heat source is used for the reference case (green line), while the 10th and 75th percentiles of heat source are implemented to see the effects of less and more heat from the waste package on near-field hydro-thermal coupled processes. Figure 2-2B shows the evolution of average temperature within the waste package from three heat sources. In all cases, the maximum temperature is reached between 10 and 20 years after the waste package is disposed of in the repository.

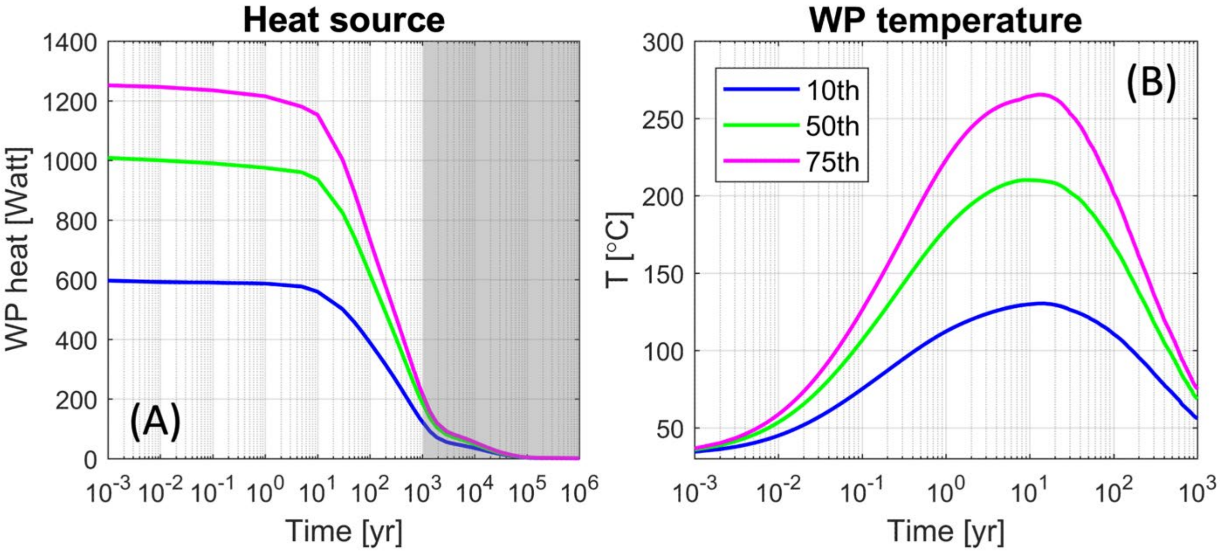

Figure 2-2. Heat source. (A) Transient decay heat curve for waste packages from the 10th, 50th, and 75th percentiles of frequency distribution of heat outputs that are predicted at the selected canisters. The heat source is scaled based on the volume of a quarter of waste package modeled in this study. (B) Temporal evolution of average temperature within waste package for three types of heat source.

2.1.3 Stress-dependent DRZ Permeability

In this reduced-order simulation, the effective stress acting on the DRZ is approximated by the temporal changes of average liquid saturation (ΔS_l) within the buffer:

$$\Delta\sigma_{eff} = 3K\Delta S_l\beta_{sw}, \qquad \text{Equation (1)}$$

Where K [Pa] is the bulk modulus of the buffer material and β_{sw} [-] is the dimensionless moisture swelling coefficient, approximately 0.238 for a bentonite buffer material (Rutqvist et al. (2011)). Corresponding evolution of the DRZ permeability as a function of the effective stress is implemented to mimic geomechanical behavior of the DRZ without implementing mechanical components explicitly. Three models have been suggested to express the changes in permeability as a function of changes in normal stress across fractures for shale rock: (1) exponential function (Dewhurst et al. (1999), Chen et al. (2015)), (2) cubic-law function (Kwon et al. (2001)), and (3) two-part Hooke's law model (TPHM) (Liu et al. (2009)). The effects of three stress-dependent permeability functions on the fluid flow and solute transport associated with the buffer-swelling process were recently investigated by Chang et al. (2021).

In this study, the TPHM is implemented within PFLOTRAN, relating DRZ permeability evolution to normal effective stress with the specified hydrological and mechanical parameter values. The concept of TPHM represents non-uniform deformation of heterogeneous rock by dividing the rock body into ‘soft’ and ‘hard’ parts to describe different stress-strain behaviors (Liu et al. (2009)). Dividing total porosity into soft and hard parts allows for the superposition of distinct relationships as functions of effective stress which combine to affect the total permeability. In relatively high effective-stress ranges, the hard part of the rock controls permeability, such that the soft part can be neglected (due to micro-crack closure at high stress conditions). The hard-part permeability can be expressed as follows:

$$\kappa_e = \kappa_{e,0}e^{-\beta c_e\phi_{e,0}\Delta\sigma_{eff}} \qquad \text{Equation (2)}$$

where κ_e [m^2] and ϕ_e [-] are the stress-dependent hard-part permeability and porosity, c_e [1/MPa] (= 0.185) is the compressibility of the hard part, and β [-] (= 12.5) is a constant stress sensitive coefficient. $\phi_{e,0}$ (= 0.2) is the hard-part porosity under zero effective stress.

In low effective-stress ranges, the permeability changes mainly due to the deformation of the soft-part porosity, which experiences relatively large deformation, even though the soft-part porosity takes a small portion of the total pore volume. Soft part permeability can be expressed as follows:

$$\kappa_t = \alpha \left[\gamma_t \exp\left(-\frac{\Delta\sigma_{eff}}{K_t} \right) \right]^m \qquad \text{Equation (3)}$$

where κ_t [m^2] is the soft-part permeability, γ_t [-] (= 0.005) is the volume fraction of the soft part under zero effective stress, α [m^2] (= 1x10^{-16}) and m [-] (= 2.0) are material constants. By superimposing the equations (2) and (3), the total permeability can be expressed as follows (Zheng et al. (2015)):

$$\kappa = \kappa_{e,0} e^{-\beta c_e \phi_{e,0} \Delta\sigma_{eff}} + \alpha \left[\gamma_t \exp\left(-\frac{\Delta\sigma_{eff}}{K_t} \right) \right]^m \qquad \text{Equation (4)}$$

The initial permeability values for the DRZ are unknown, such that the values are assigned as a constant value for the reference case (one order of magnitude less than that of the shale host rock) or computed under assumption that the DRZ permeability will approach that of the host rock as buffer swelling stress reaches the maximum. Note that the DRZ may not completely revert to the intact state by swelling due to inelastic behaviors of fractures and rock matrices, but this assumption provides a physically reasonable endpoint permeability considering the mechanical evolution of the DRZ.

2.1.4 Saturation-temperature-dependent Thermal Conductivity

To describe the impacts of the heat pulse on the thermal characteristics of the material, this study implements the saturation-temperature-dependent effective thermal conductivity that can be defined by wet (water-saturated) and dry thermal conductivities with the power-law function as follows (Somerton et al. (1974)):

$$K_{T,eff}(S_l, T) = \left[K_{T,dry} + \sqrt{S_l \left(K_{T,wet} - K_{T,dry} \right)} \right] \left(\frac{T - T_{ref}}{300} \right)^{\gamma} \qquad \text{Equation (5)}$$

where $K_{T,eff}$, $K_{T,dry}$, $K_{T,wet}$ [W/m/K] are effective, dry and wet thermal conductivities, respectively, T_{ref} is the reference temperature (T_{ref} = -273.15°C), and γ is the exponent of temperature (γ = -1.18). Figure 2-3 shows the change of effective thermal conductivity as a function of liquid saturation and temperature. The reference case neglects the temperature dependence by turning off the temperature term in Equation (5), which is shown as a solid black line in Figure 2-3.

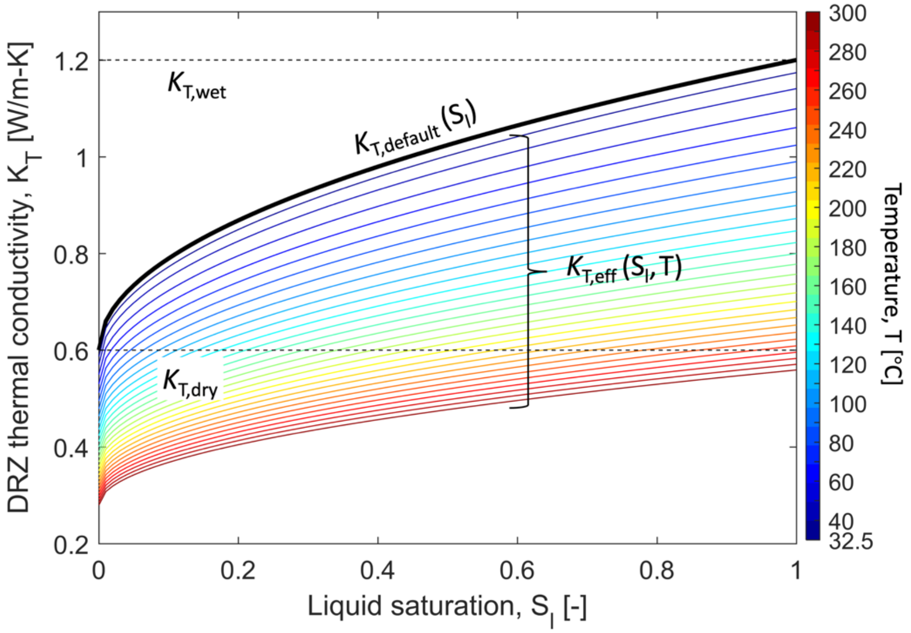

Figure 2-3. Thermal conductivity changes as a function of liquid saturation and temperature. The values of dry and wet thermal conductivities are for the DRZ in this study. The solid black line represents the default thermal conductivity independent of temperature changes.

2.2 Results

2.2.1 Effect of Buffer Swelling

The simulation results show that the canisters containing heat-emitting nuclear waste will perturb the thermal field around the repository (Figure 2-2B), which will affect the rate of re-saturation of the buffer. As the water inflow into the surrounding buffer and DRZ initiates, the swelling stress in the buffer is assumed to be equivalent to the normal stress acting on the DRZ over time (Figure 2-4). The TPHM permeability function reduces DRZ permeability slightly, retarding re-saturation of the buffer (orange line), compared to the reference case of constant permeability (black line).

Including thermal impacts on heat conduction reduces effective thermal conductivity of the buffer and DRZ, as shown in Figure 2-3, and more heat will be confined within the waste package. Consequently, water can penetrate into the DRZ more rapidly, so that faster re-saturation is observed (green line in Figure 2-4). The amount of heat generated from the waste package has a greater impact on buffer swelling than hydro-thermo-mechanical characteristics of the material does (blue, green, and magenta lines for 10th, 50th, and 75th percentiles of heat source, respectively). The greater thermal energy enhances the mobility of the liquid phase by decreasing its viscosity, facilitating water inflow into the buffer and DRZ (quicker decrease of gas saturation; magenta line in Figure 2-4). The divergence of buffer swelling stresses from the five cases indicates the impacts of thermo-hydro-mechanical behaviors of the repository system as well as the amount of heat energy on near-field coupled heat and fluid flow. Once the buffer is entirely saturated with water, swelling stresses and saturation will converge to the saturated conditions with heat decay.

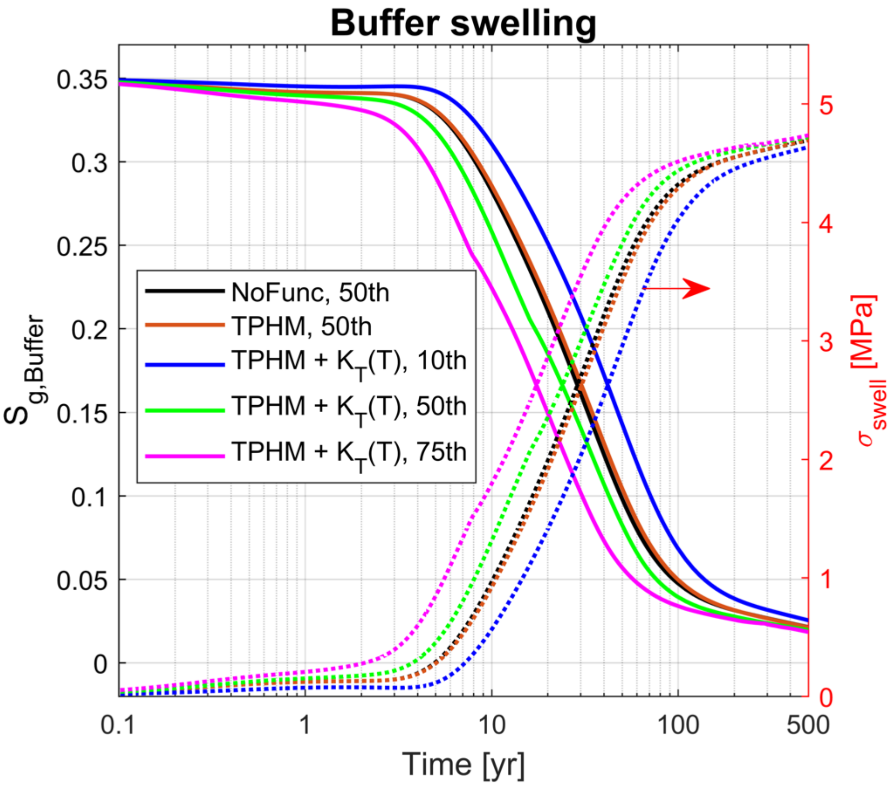

Figure 2-4. Evolution of gas saturation (solid line) within the buffer and corresponding changes in swelling stress (dashed line) acting on the DRZ for five cases: (1) no permeability and temperature-dependent thermal conductivity functions (reference case; black), (2) TPHM without temperature-dependent thermal conductivity (orange), and (3 to 5) TPHM and temperature-dependent thermal conductivity with variation in heat sources of 10th, 50th and 75th percentiles (blue, green, and magenta, respectively).

2.2.2 Swelling-driven Changes in Physical Quantities

Figure 2-5 shows the temporal evolution of average pressure, mobility, and saturation of the liquid phase; gas saturation; temperature obtained at the DRZ; and the permeability calculated from the equation (4). The variation in material characteristics and heat source determines the thermal gradients as well as the mobility of liquid phase ($\lambda_l = \kappa_{rl}/\mu_l$) that will influence the temporal distribution of gas and liquid saturation and corresponding pressurization (Figure 2-5A to Figure 2-5E), eventually changing the DRZ permeability (Figure 2-5F).

Under our model setting of the same initial DRZ permeability, swelling-driven permeability reduction may not have significant impacts on fluid flow and heat transfer (orange and black lines). Temperature-dependent thermal conductivity lessens to 0.9 W/m-K at the fully saturated condition of the host rock (approximately 25% less than the wet thermal conductivity; Figure 2-3) as the temperature increases, which confines heat from the waste package more effectively and simultaneously increases the mobility of liquid phase. Thus, higher temperature and faster increases of liquid saturation are observed compared to the reference case (green lines). Once the re-saturation process starts with heat pulse (Figure 2-5D and Figure 2-5E), the stress-dependent TPHM function reduces the DRZ permeability (after about 2.5 years of simulation; Figure 2-5F).

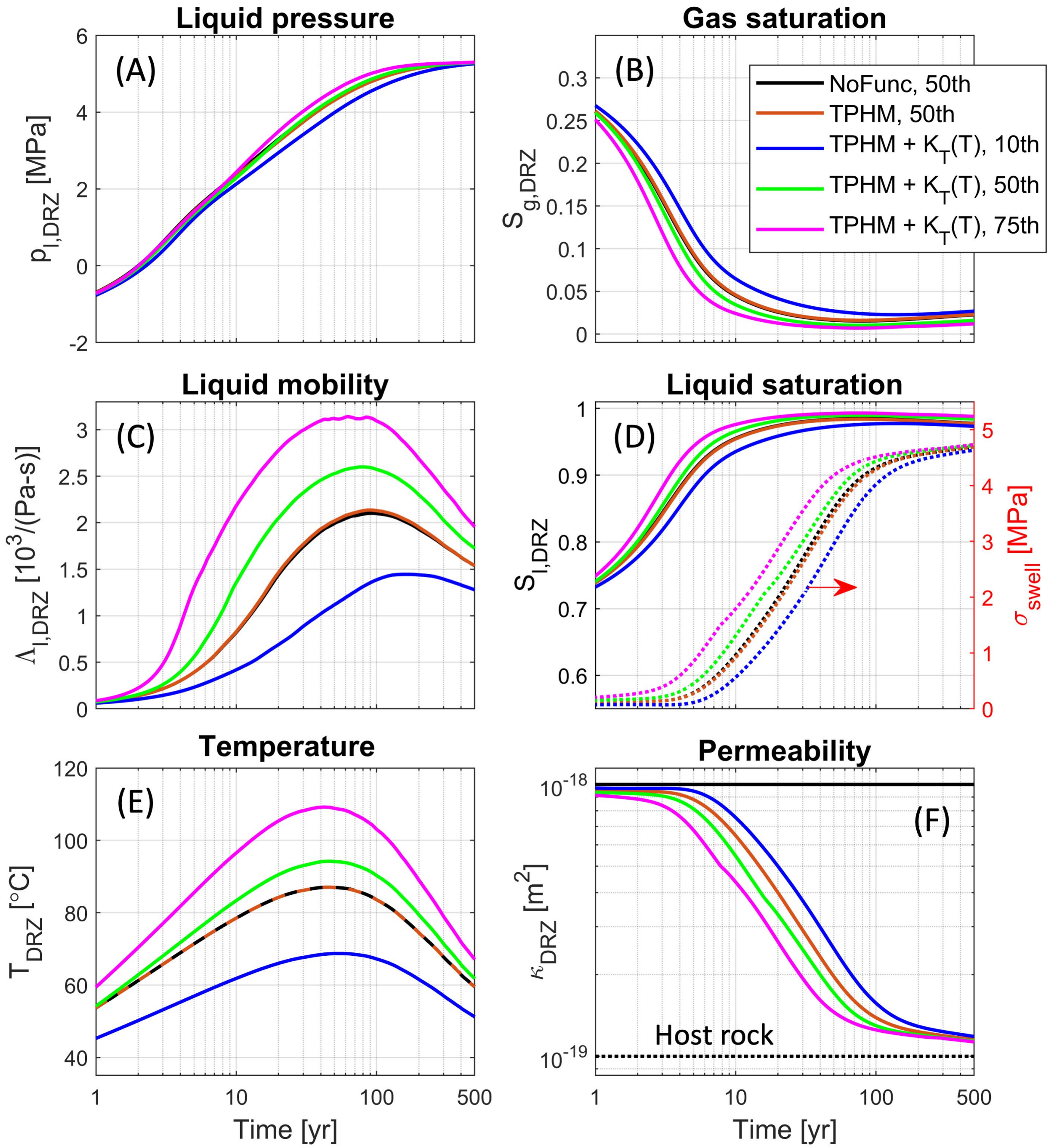

Figure 2-5. Evolution of average physical quantities within the DRZ for five cases: (A) liquid pressure, (B) gas saturation, (C) liquid mobility, (D) liquid saturation and swelling stress, (E) temperature, and (F) permeability. The host rock permeability values ($1x10^{-19}$) are indicated by a black dashed line in figure F.

Simulation results indicate that the amount of heat energy generated from the waste package plays a critical role in fluid flow and heat transfer, potentially determining the level of buffer swelling impacts on the DRZ as the DRZ resaturates.

Figure 2-6 shows the spatial distribution of temperature, mobility, velocity in x-direction ($u_{l,x}$), and saturation (S_l) of the liquid phase at t = 60 years for three types of heat sources. The greatest heat source (75th percentile) causes the largest increase of temperature in the repository system (Figure 2-6C) that leads to the largest mobility of liquid phase ($\lambda_l = 5.3x10^3$ 1/(Pa-s) in the DRZ; Figure 2-6F) and rapid re-saturation of the buffer and DRZ (Figure 2-5D) due to faster inflow from the saturated host rock (negative $u_{l,x}$ in Figure 2-6G to Figure 2-6I). At the same time, the presence of a heat source generates thermal gradients, which can influence the directional fluid flow and re-saturation process locally.

For the case of the 75th percentile of heat source, strong thermal gradients can enhance the outward fluid flow as indicated by the positive $u_{l,x}$ in the buffer nearest the waste package (warm color in Figure 2-6I), which will develop countercurrent flows in the near-field. On the other hand, water inflow is still dominant at the region less affected by heat loading (e.g., buffer between waste packages), which results in faster re-saturation (Figure 2-6J to Figure 2-6L). Also, stronger heat emission causes further reduction of thermal conductivities of the engineered and natural barriers, which will limit heat conduction out of the waste package. Thus, heat remains strong at the adjacent buffer that can delay the re-saturation process of the buffer nearest the waste package (Figure 2-6J to Figure 2-6L). This localized effect of thermal characteristics maintains high temperature and develops prolonged dry-out conditions within in the waste package.

Likewise, heat flow will be governed by the balance between convection and conduction determined by local temperature fields for the energy conservation. In a relatively short time frame (less than 1000 years), three major flow dynamics are engaged in the near-field; (1) heat-driven thermal gradients develop outward fluid flow nearby the waste package in positive lateral directions, (2) water flows into the unsaturated DRZ nearby the host rock in negative directions, and (3) reduction of thermal conductivity limits heat conduction into the engineered barrier system.

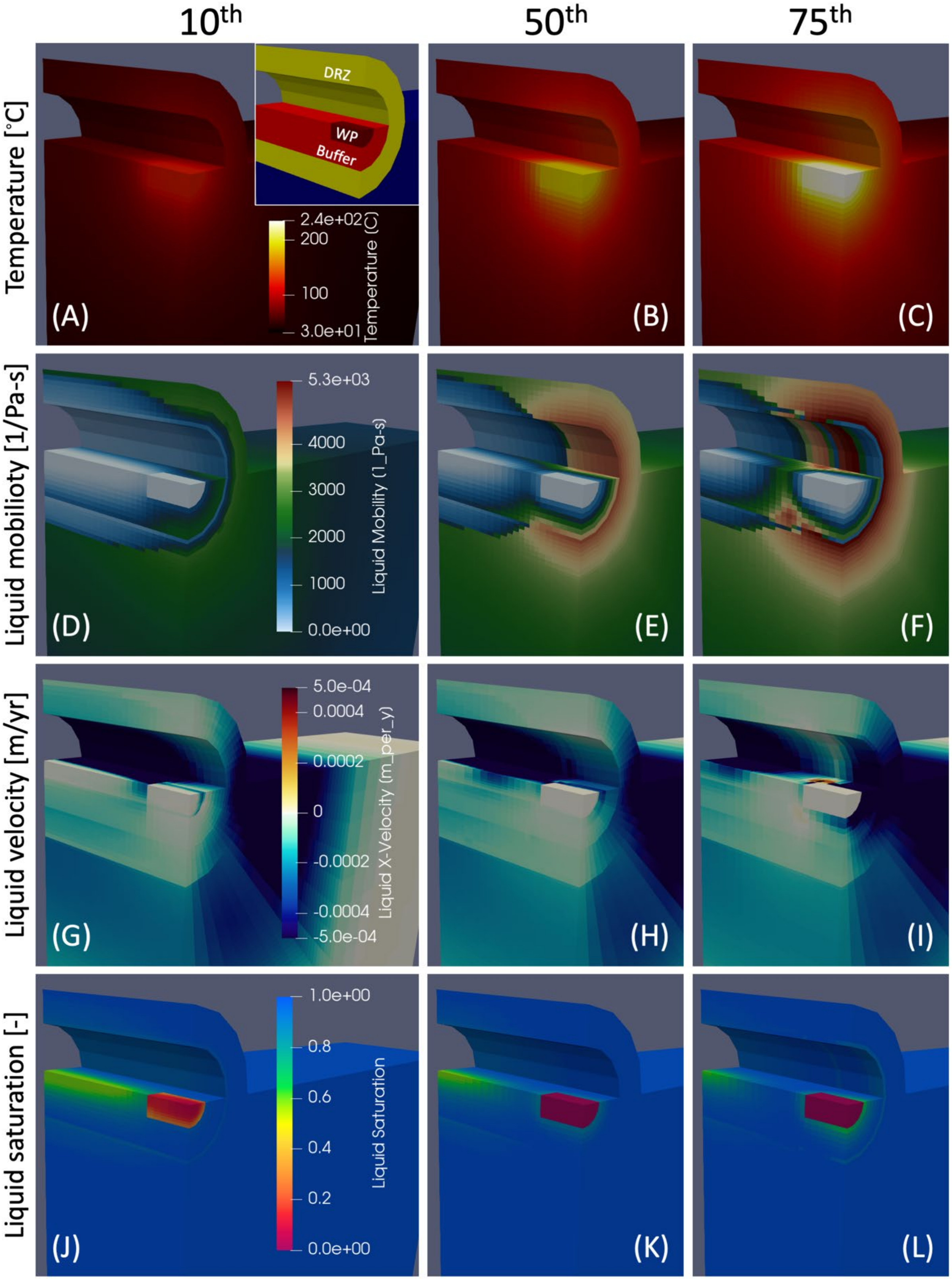

Figure 2-6. Spatial distribution of (A to C) temperature, (D to F) liquid mobility, (G to I) velocity in x-direction, and (J to L) liquid saturation at t = 60 years for the three heat sources. The inset figure in figure A shows the sections of model domain.

2.2.3 Impact of Numerical Domain Dimension

For the near-field analysis, the model domain is vertically shortened to reduce the numerical cost and both top and bottom boundaries are set to open boundary conditions to resolve the boundary effects potentially caused by the domain geometry. However, the reduced domain may not describe the full physics of near-field hydro-thermal behaviors because of limiting heat diffusion from the source to greater distance. Thus, we extend the model domain vertically from the surface to a depth of 1 km, which is similar to the vertical scale of the field-scale performance assessment model domain (Figure 2-7). Note that the vertically extended domain has the same location of the waste package, material properties, and hydraulic/thermal gradients for initial conditions to ones used in the reference model (Figure 2-1), such that this comparative study will reveal the effect of the vertical extent of the model domain on the near-field behaviors.

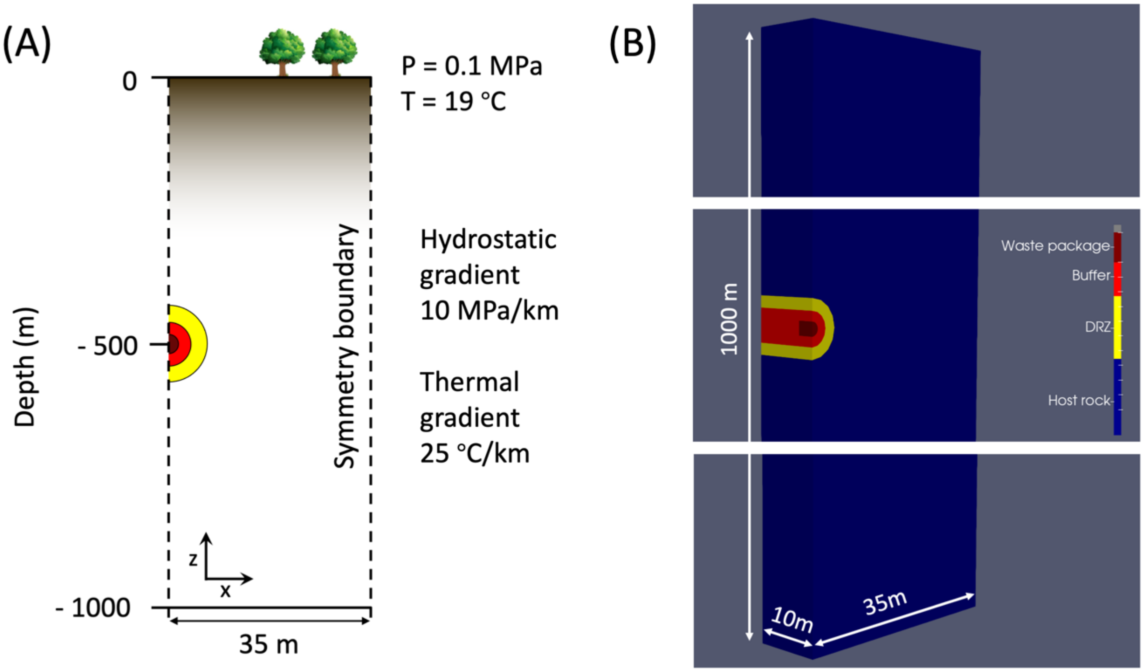

Figure 2-7. Model description and setting. (A) Schematic description (not to scale) of the vertically extended model domain consisting of waste package, buffer, DRZ, and shale host rock. (B) Numerical domain and geometry.

Figure 2-8 compares average temperature, mobility of liquid phase, liquid saturation, and swelling stress within the buffer and the DRZ for the DPC representative of the 50th percentile of heat outputs with both the reduced (green) or extended (purple) model domain. During the phase of heat emitting, the thermally driven fluid flows accelerate the re-saturation process and saturate both buffer and DRZ with over 90% liquid phase until the temperatures reach the maximum. The vertically short or extended domain generate similar thermal impacts during this period as shown in Figure 2-8A and Figure 2-8B. Once the temperatures peak, the extended domain delays the relaxation of heat (purple lines; Figure 2-8A and Figure 2-8B). Within the buffer, the liquid mobility continues to increase gradually throughout the simulation, but with a slower rate, corresponding to the delayed cooling in the extended domain (purple; Figure 2-8C). The DRZ also has a larger fluid mobility after 100 years compared to one from the short domain, and the mobility decreases with heat decay (Figure 2-8D).

Once temperatures start to decline, the extended domain delays the relaxation of heat within the buffer and DRZ that may cause variation in thermal impacts on near-field flow and transport characteristics

(Figure 2-8C and Figure 2-8D). However, both materials are nearly fully saturated, so this does not cause large differences in liquid saturation between two domains (Figure 2-8E and Figure 2-8F).

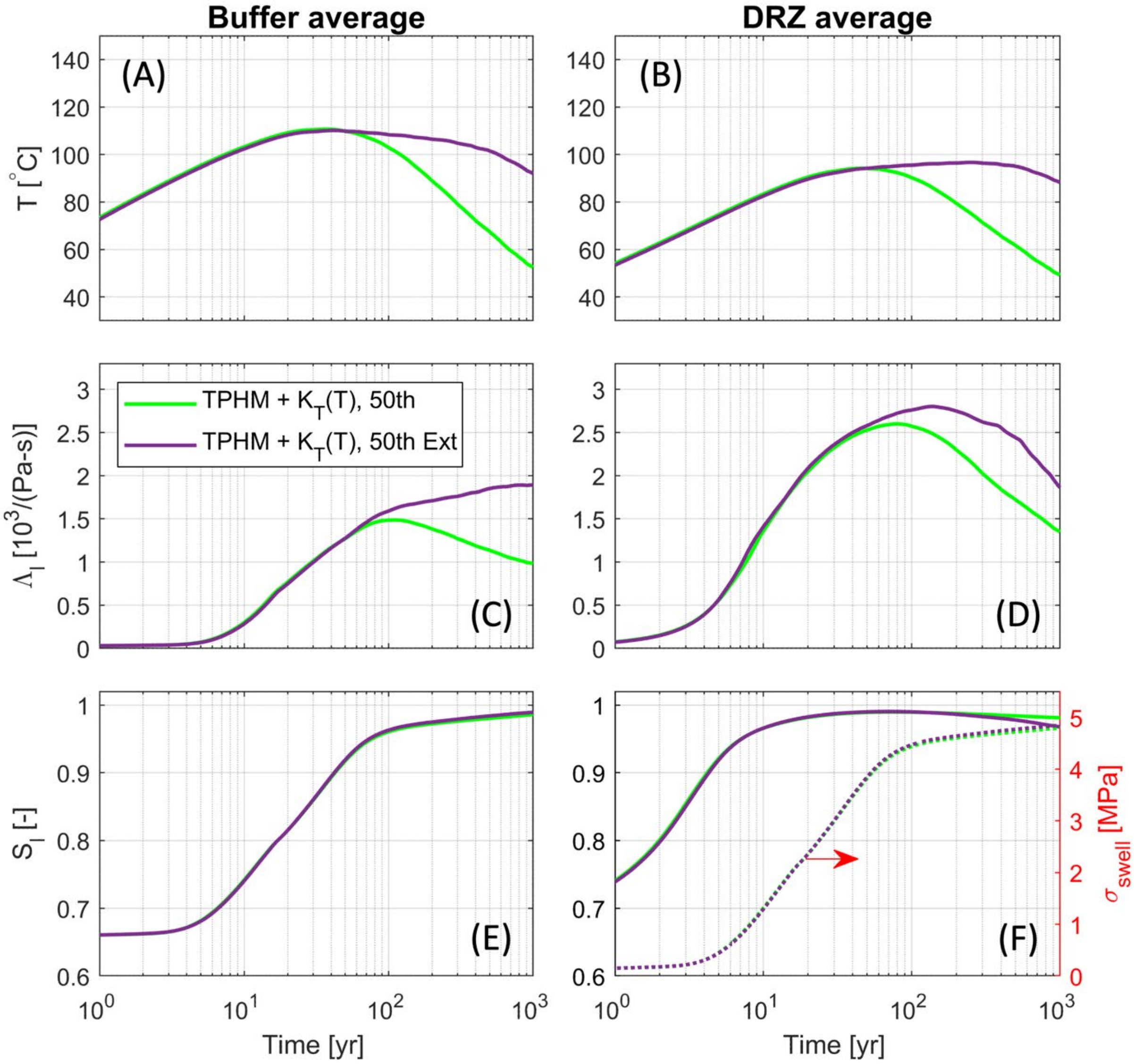

Figure 2-8. The effect of model domain size. Temporal evolution of average (A to B) temperature, (C to D) mobility of liquid phase, and (E to F) liquid saturation within the buffer and DRZ for the case of 50th percentile of heat output with a vertically reduced and extended domain.

2.3 Findings and Future Works

This generic study shows that heat-driven perturbations in hydro-thermal characteristics of the shale-hosted geologic repository system and their impacts on near-field heat and fluid flow can be captured by implementing saturation-temperature-dependent functions of permeability and thermal conductivity. In the near-field region, the amount of heat emitted from the waste package plays a significant role in controlling the multiphysics coupled response to the buffer swelling. The greater heat will generate (1) larger mobility of liquid phase that accelerates inflow into the unsaturated buffer and DRZ from the fully saturated host rock, (2) steeper thermal gradients that can result in outward flow within the buffer and DRZ nearest the waste package, and (3) smaller thermal conductivity that confines more heat within the buffer.

This type of reduced-order model could be used to integrate the effects of multiphysics coupling processes in the near-field into a field-scale performance assessment model corresponding to sequential phases of thermal and mechanical loading-unloading. For the future work, we will continue

1. To investigate the boundary effects of the model domain
2. To analyze the effect of geological heterogeneity in shaly formations (e.g., interbedding)
3. To simulate other types of geologic repository systems (i.e., crystalline, salt rock, unsaturated alluvium layers) to see hydro-thermal behaviors in the near-field.

This page is intentionally left blank.

3. THERMO-MECHANICAL ANALYSIS OF SALT REPOSITORY

This section describes continued thermal creep modeling of a generic salt repository with realistic thermal histories of DPCs. Salt host formations are of interest for disposition of heat generating waste due to salt's high thermal conductivity and low porosity and permeability. Because consolidation of the backfill occurs relatively quickly, peak near field temperatures are less dependent on creep parameters. The time to complete consolidation impacts only the initial rise in temperature of the canister which in all cases is less than the time to peak temperature. Thus, somewhat obviously, the near field temperature is most impacted by salt's thermal properties, in particular the thermal conductivity. Much of the thermal modeling in literature rely on the thermal property experiments conducted by Bechthold (2004) for model inputs. This does not take into account the variability that could arise due to host salt purity and potential non heterogeneity. The purpose of this study was to determine the effect of possible thermal conductivities on near field temperature.

3.1 Background

There have been numerous studies to quantify temperature-dependent thermal conductivity of solid geological rocksalt and crushed run of mine backfill. Rocksalt is comprised of halite, anhydrite, poly halite and other water insoluble impurities with purity ranging from nearly 100% halite in domal formations to 95% in bedded formations. Bedded formations can also have spatial non heterogeneity but would likely be avoided in repository siting. A chart of salt thermal conductivity as a function of temperature from a number of experimental studies is taken from Bauer and Urquhart (2014) and shown in Figure 3-1. The highest reported values are expectedly produced by testing of single crystal samples and testing of Avery Island salt which is a domal formation of very high purity.

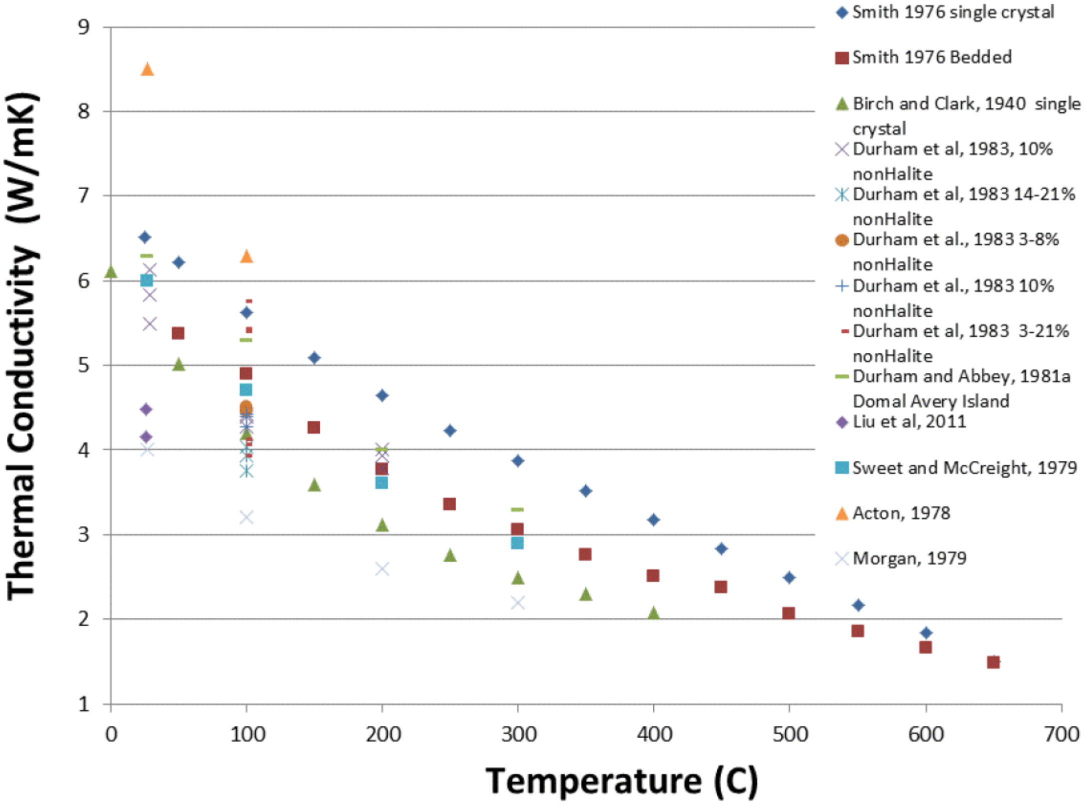

Figure 3-1. Temperature-dependent thermal conductivity data from previous works. (Credit: Bauer and Urquhart, 2014)

Much of the literature involving thermal analysis of heat-generating waste in a salt repository utilizes two sources to account for temperature-dependent thermal conductivity, Equations 6 and 7 presented by Bechthold (2004), and Equation 8 from Munson (1990), where T is the temperature (Celsius in Eq. 6 and Kelvin in Eq. 7), φ is the dimensionless porosity, and $K_{T\text{-}300}$ is the thermal conductivity at 300 K (5.4 W/m^3 as reported by Munson (1990)). Bechthold (2004) conducted experiments on domal salt from the Asse Salt Mine and Munson (1990) conducted experiments on bedded Permian salt from the Waste Isolation Protection Plant (WIPP). The predicted values from both are in close agreement, but as shown in Figure 3-1, there is a fair amount of scatter in other experimental values.

$$K_{th}(T\ [°C]) = 5.734 - 0.01838\,T + 0.0000286\,T^2 - 1.51 * 10^{-8}\,T^3 \qquad \text{Equation (6)}$$

$$K_{crushed}(\varphi) = K_{th}(T)[1 + 0.3\varphi - 27.2\varphi^2 + 74\varphi^3 - 54\varphi^4] \qquad \text{Equation (7)}$$

$$K_{th}(T\ [K]) = K_{T-300}\left(\frac{300}{T}\right)^{1.14} \qquad \text{Equation (8)}$$

Bauer and Urquhart (2014) represented bulk crushed salt thermal conductivity as the geometric mean of a two-medium material as suggested by Ingebritsen et al. (2006, citing Sass et al., 1971), Equations (9) and (10). The two mediums are salt, properties taken as a single halite crystal, and air. n is the porosity, and K_b, K_r, and K_f, are the bulk rock, and fluid thermal conductivities respectively. The temperature-dependent conductivity air and halite are shown in Equations 11 and 12.

$$K_b = K_r^{1-n} K_f^{n} \qquad \text{Equation (9)}$$

$$K_{crushed} = K_{air}^{1-n} K_{halite}^{n} \qquad \text{Equation (10)}$$

$$K_{air}(T\ [°C]) = 1.52\ \times 10^{-11}T^3 - 4.8574 \times 10^{-8}T^2 + 1.0184 \times 10^{-4}T - 0.00039333 \qquad \text{Eq. (11)}$$

$$K_{Halite}(T\ [°C]) = -1.3264\ \times 10^{-7}T^3 + 9.6384 \times 10^{-5}T^2 - 3.0867 \times 10^{-2}T + 6.8077 \qquad \text{Eq. (12)}$$

The purity of the host salt would intuitively have an impact on thermal conductivity with anhydrite and polyhalite being roughly 80 and 20% less conductive than halite, respectively; WIPP salt has been shown to have between 1% and 5% impurities by weight. The polycrystalline nature of salt formations has little impact on thermal properties so long as the crystals are in contact with one another, but this can be disturbed by mechanical or thermal processes that cause fractures in the host rock. Mellegard et al. (2013) noted that at elevated temperature bedded Permian salt begins to fracture (explosively at very high temperatures) as temperature increases. The driver for this behavior is primarily increased pressure in the fluid inclusion sites. The samples that did not violently decrepitate were subjected to uniaxial strain for the purpose of determining mechanical properties. Bauer and Urquhart (2015) measured thermal conductivity on these samples and noted conductivity was 10-50% less than non-fractured samples of similar porosity. This suggests a sufficiently dense fracture network is an additional mechanism that could alter bulk thermal conductivity. In simulations performed by Rutqvist and Tounsi (2021) thermal pressurization results in pore pressure beyond the lithostatic stress which induces hydraulic damage. This type of hydraulic damage may not resemble the dilated samples, but a sufficiently dense fracture network has the potential to negatively impact thermal conductivity

3.2 Model Description

FLAC V7.0 (Itasca 2011) was used for 2-D plane-strain simulation of a waste package surrounded by crushed salt backfill within a rectangular tunnel opening. The constitutive laws for crushed and intact salt were *cwipp* and *pwipp*, respectively, which are built-in FLAC viscoplastic models based on an early creep law (Senseny 1985). Jones et al. (2021) showed that artificially reducing the creep rate by 20 and 30%

had minimal effect on near field peak temperature. Since backfill consolidation occurs in less than 100 years for even the most decreased creep rate case, there is only so long for the insulating effect of crushed salt backfill to increase waste package temperatures. Once consolidation occurs, thermal conductivity of the drift zone is similar to that of the intact host salt. Time to consolidation, be it 25 or 50 years, has minimal impact on near field peak temperatures. Due to this, the choice of constitutive creep law is not critical to this study.

Thermal Conductivity

As seen in Figure 3-1, measured thermal conductivity varies from about 4.0 to 8.5 W/m-K at 20°C, and 2.5 to 4.75 W/m-K at 100°C. The widely accepted Bechthold equation is likely a very good approximation for modeling hypothetical repositories, but it seems thermal conductivity can be site specific, spatially dependent in the formation, or affected mechanical damage.

Thermo-mechanical modeling studies were done in 2D to investigate how sensitive the temperature evolution is to possible variability in temperature-dependent thermal conductivity. A selection of published empirical equations for halite thermal conductivity are shown in Figure 3-2. Smith (1976) evaluated the use of the laser flash thermal diffusivity method on single crystal halite, but acknowledged deficiencies of this method and claimed error of about ± 10%. Bauer and Urquhart (2014) is one of the more recent test series on single crystal halite. Paneru et al. (2018) measured the same samples as did Bauer and Urquhart but found different results. The Bechthold (2004) equation is also plotted.

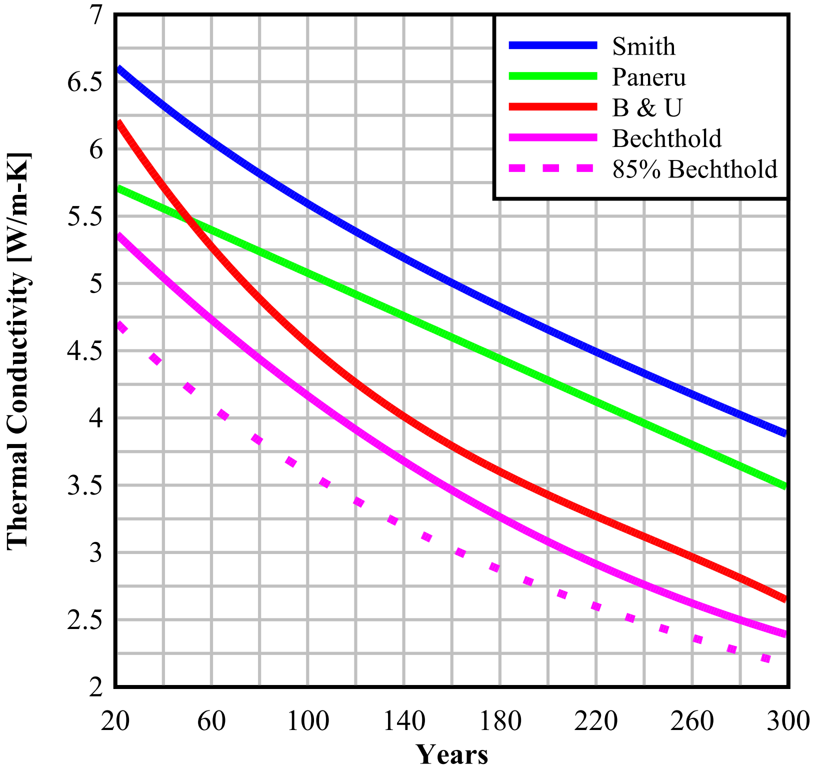

Figure 3-2. A selection of temperature-dependent thermal conductivity relationships available in literature.

While not realistic, the most thermally conductive scenario would be if the host formation had the same conductivity of a single halite crystal. Values reported by Smith (1976) were taken as the upper possible limit, despite the acknowledged error, because it encompasses the results from Bauer and Urquhart (2015) and Paneru et al. (2018) which used the same sample. The Bechthold (2004) results are taken as the standard on which to compare. It was difficult to derive a justifiable lower limit from literature, so an arbitrary 85% of Bechthold was used.

Temperature dependent thermal conductivity was incorporated using an intrinsic FLAC function (th_general) which accounts temperature dependence in the form of Equation 13. The constants C_1, C_2, and λ were calculated so that Equation 13 was fit to the Smith (1976), Bechthold (2004), and 85% of the Bechthold data.

$$K_{th} = C_1 + C_2 \left(\frac{300}{T}\right)^{\lambda} \qquad \text{Equation (13)}$$

The th_general constitutive model for heat conduction updates the thermal conductivity as a function of temperature while cycling but does not do so as a function of porosity in the backfill. The backfill thermal conductivity must be updated at manual intervals which interrupts the code and has a negative impact on code execution time. The script to update backfill thermal properties was updated in FY22 which reduced code execution time compared to FY21. This allowed for a reduction in the update interval and resulted in more finely resolved temperature histories, and the extension of simulation time. The update interval is shown in Table 3-1.

Table 3-1. Comparison of the backfill temperature and porosity dependent thermal conductivity update interval between FY21 and FY22.

Time (years)	FY21 Update Interval [Years (hours)]	Update Interval [Years (hours)]
0-2	0.05 (438)	0.008 (70)
2-3	0.05 (438)	0.023 (200)
3-20	0.2 (1753)	0.023 (200)
20-25	0.5 (4380)	0.023 (200)
25-40	0.5 (4380)	0.046 (400)
40-60	1 (8760)	0.046 (400)
60-80	2 (17520)	0.046 (400)
80-100	5 (43800)	0.046 (400)
100-160	5 (43800)	0.08 (700)
160-190	10 (87600)	0.08 (700)
190-310	10 (87600)	0.16 (1400)
310-1000	-	0.16 (1400)

Other Inputs

A specific heat value of 900 J/kg-K was selected based on similar values reported by Bechthold et al. (2004) for both intact and crushed salt. Bauer and Urquhart (2015) reported values up to around 1080 J/kg-K for a single halite crystal. A single case with the specific heat set to 1100 J/kg-K was executed and resulted in a difference in peak temperature of 3 K. All other simulations used 900 J/kg-K.

Salt thermal expansivity of 13.83×10^{-5}/K (volumetric) was obtained from Robinson (1988, Table 9, halite). The coefficient of linear thermal expansion is one third of this value. The corresponding reported density value is 2.163 Mg/m^3, which is about 3% larger than the value of 2.100 Mg/m^3 used in this study.

Creep properties were taken from Itasca (2011) for the *pwipp* and *cwipp* models; these property values are attributed to Senseny (1985). Initial backfill porosity was set to 36%, consistent with estimates for porosity of granular materials. This value is the minimum reported porosity for a closest packing of uniform spheres. Similar in situ porosity values for crushed salt (35% to 38%) were reported by Bechthold et al. (2004).

Grid Size and Resolution

Jones et al (2021) showed that a vertical domain of 150 m above and below the waste package was sufficient given peak temperature occurs at less than 300 years. The linear heat rate is scaled to 30 m to represent packages spaced 30 m apart center to center. The horizontal domain is 15 m with the center of the canister at the origin; half symmetry is used to represent drift spacing of 30 m.

The FY21 report used a uniform grid with a cell size of 1 m with the same model extents discussed above. This study used a non-uniform mesh where all cells increase in size with distance from the waste package, and a region of smaller cells near the drift. Two meshes were generated and are shown in Figure 3.3. For ease of comparison, mesh 2 is reflected across the y-axis and plotted beside mesh 1. The majority of results were generated using mesh 1. Mesh 2 is of a finer resolution and was used to informally establish grid independence.

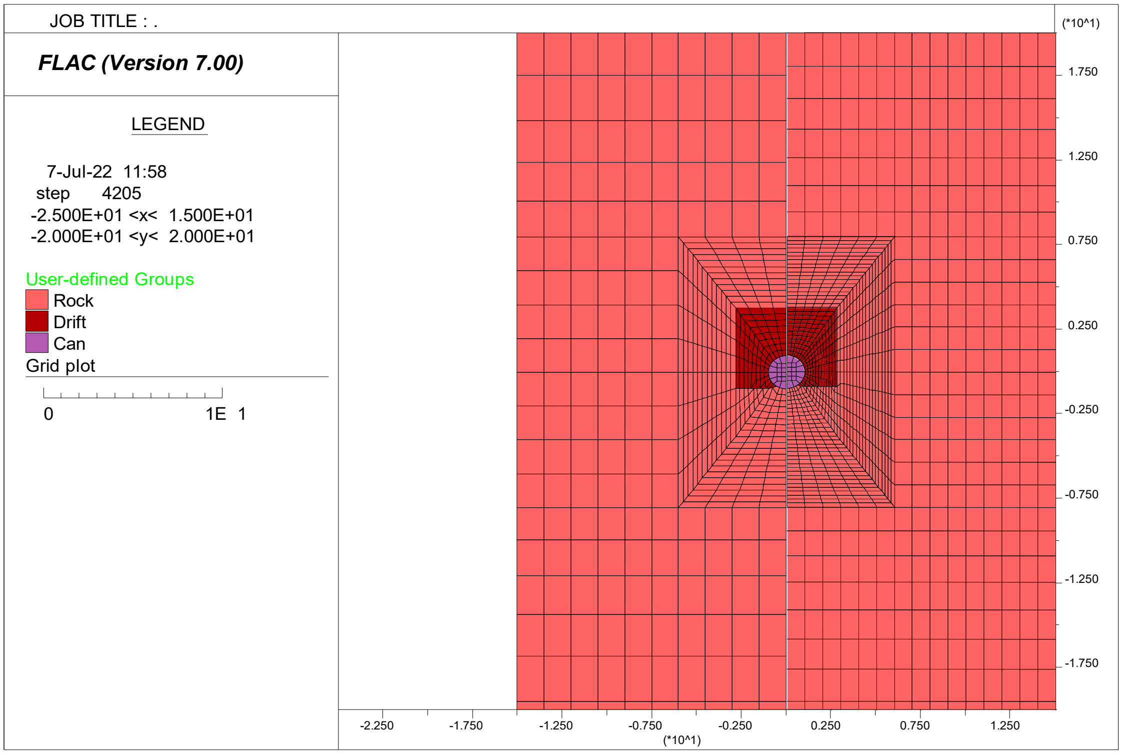

Figure 3-3. Plot of a zoomed-in portion of the model domain. Mesh 1 is plotted from x = -15 to x = 0. Mesh 2 is plotted from x = 0 to x = 15.

Figure 3-4 shows the temperature and y-displacement histories for the 75th percentile DPC generated using mesh 1, mesh 2, and the uniform mesh from FY21. The temperature results from mesh 1 and 2 are in close agreement, and the uniform mesh shows higher temperatures of about 5 K. There is some deviation in vertical displacement which may indicate further refinements are needed to accurately capture the mechanical response, but the time to complete consolidation is nearly the same. As this analysis was focused on the thermal response, further grid refinements were not made, and analysis continued with mesh 1.

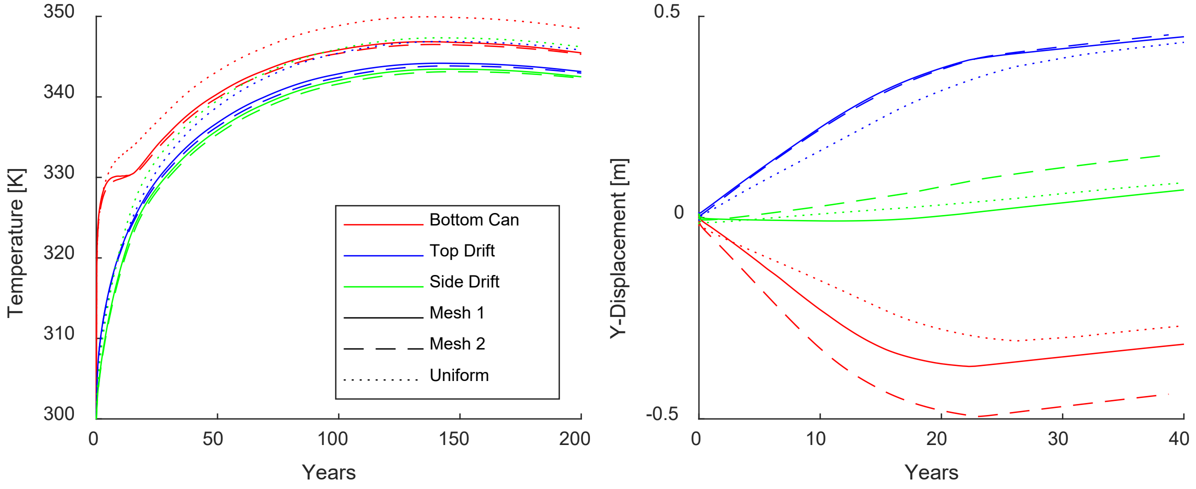

Figure 3-4. Temperature and displacement histories for the 75th percentile DPC generated with mesh1, mesh 2, and the uniform mesh from FY21.

Decay Heat

The decay heat percentiles are the same as used in the FY21 report (Jones et al. 2021) and are shown here in Table 3-2. They were compiled from the UNF-ST&DARDS database and associated software tools (Banerjee et al. 2016; Clarity et al. 2017).

Table 3-2. DPCs selected to represent percentiles of heat output.

Calendar	99th (Watts)	95th (Watts)	90th (Watts)	75th (Watts)	50th (Watts)	10th (Watts)
2100	8,034	6,764	6,058	5,006	4,034	2388
2110	7,353	6,159	5,570	4,611	3,744	2239
2130	6,317	5,249	4,828	4,009	3,297	2006
2150	5,583	4,614	4,303	3,583	2,975	1834
2170	5,045	4,156	3,919	3,271	2,735	1704
2200	4,465	3,673	3,506	2,934	2,470	1557
2250	3,829	3,156	3,051	2,563	2,170	1384
2300	3,399	2,813	2,740	2,307	1,957	1257
2400	2,814	2,350	2,303	1,945	1,653	1071
2500	2,409	2,029	1,989	1,683	1,431	932
2750	1,749	1,504	1,459	1,236	1,055	693
3000	1,339	1,177	1,123	952	815	539
3500	882	810	745	631	545	366
4000	668	636	567	481	418	284
5000	506	502	433	367	321	223
6000	449	451	385	327	286	201
8000	388	393	333	283	248	176
10000	342	348	294	250	219	158
15000	256	264	220	189	165	123
20000	199	207	171	147	128	98
30000	131	138	113	97	85	67

Calendar	99th (Watts)	95th (Watts)	90th (Watts)	75th (Watts)	50th (Watts)	10th (Watts)
40000	94	99	81	70	61	49
60000	56	58	47	41	35	29
80000	37	37	31	27	23	18
100000	27	26	22	19	16	13
150000	19	16	14	12	10	7
200000	17	14	13	11	9	6
300000	16	13	12	10	9	6
400000	15	12	11	10	8	6
500000	14	11	11	9	8	5
750000	11	9	9	8	6	4
1000000	10	8	8	7	6	4

Selected DPCs:

	Location	**DPC ID**	**Loaded Date**
99th:	Crystal River ISFSI	CR3-32PTH1-L-2D-W-13	06/01/07
95th:	Browns Ferry ISFSI	MPC-89_4803D_MPCFW045	06/08/17
90th:	Turkey Point ISFSI	DSC-32PTH_1803D_32PTH-032-C-1	10/26/11
75th:	Waterford ISFSI	MPC-32-MPC-224	04/01/12
50th:	Arkansas Nuclear ISFSI	MPC-24-MPC-003	12/13/03
10th:	San Onofre ISFSI	24PT1_4701D_DSC009	12/01/03

3.3 Results and Discussion

Figure 3-5 shows results for the 95th, 90th, 75th, 50th, and 10th percentile waste packages while using the Bechthold equations for thermal conductivity. The right side of each plot shows a sub-plot outlined in red of the first 25 years of simulation time. In each simulation the waste package temperature increases dramatically then levels as the backfill consolidates and conducts more heat from the waste package. In the displacement plots, the inflection point (most easily seen in the 95th percentile case) represents when the backfill has consolidated or nearly so. This is the point where consolidation is no longer a major contributor to vertical displacement, and displacement at all three locations is positive due to thermal expansion driving the domain towards the free surface.

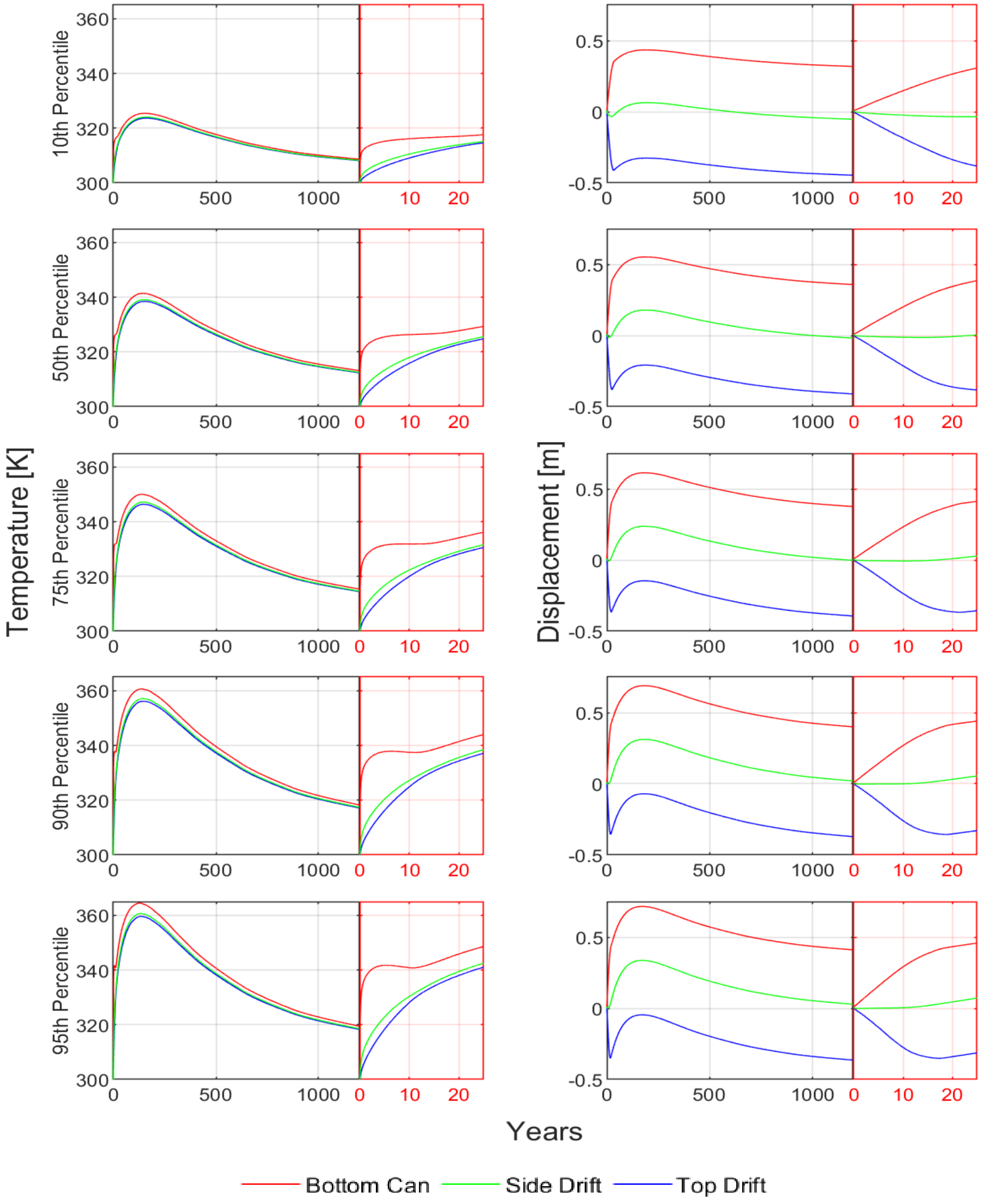

Figure 3-5. Temperature and y-displacement histories for the 95th, 90th, 75th, 50th, and 10th percentile DPCs. The red box on the right side of each plot shows early behavior from 10 to 25 years.

To investigate the effect of thermal conductivity, three different temperature dependent thermal conductivity equations were used, referred to as Base, Upper, and Lower to model the temperature at three different locations: the bottom of the waste package, the top of the drift, and the left side of the drift. The Base Case is derived from Bechthold, the Upper Case from Smith, and the Lower Case is 85% of the Bechthold values. These three cases were executed for the 50th, 75th, and 95th percentile DPCs.

Temperature histories are plotted in Figure 3-6, and peak values are tabulated in Table 3-3. The results are as expected with the Upper Case generating the lowest temperatures and the Lower Case the highest temperatures. The Upper Case, which could be described as overly optimistic, results in at most a 10° reduction in max drift wall temperature compared to the base case. The lower case also results in only a 7° increase in temperature compared to the base case.

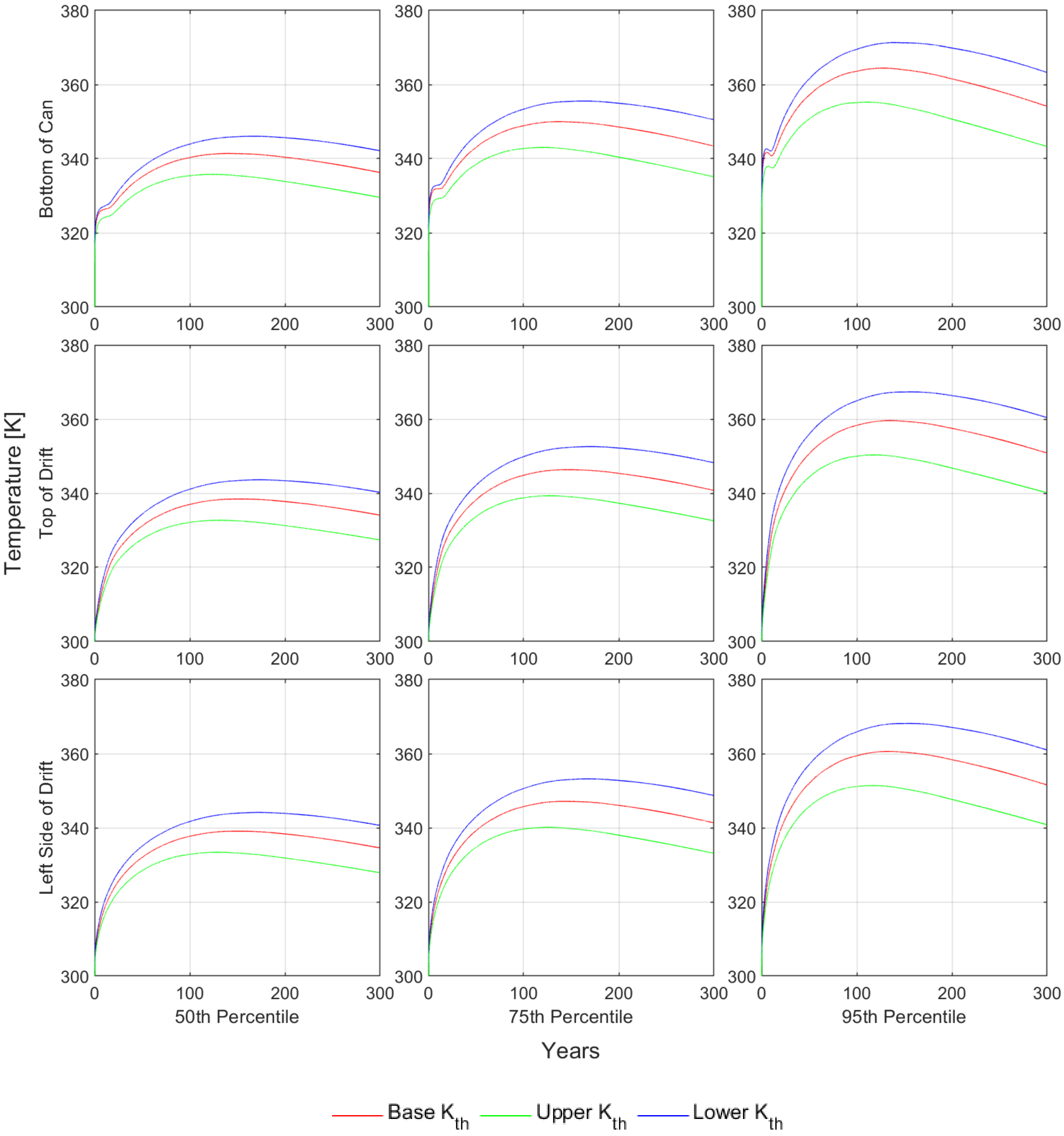

Figure 3-6. Temperature histories for the 95th, 75th, and 50th percentile DPCs using three different temperature dependent thermal conductivity equations referred to as Base Case, Upper Case, and Lower Case.

Table 3-3. Peak near field temperatures for the 95th, 75th, and 50th percentile DPCs using three different temperature dependent thermal conductivity equations referred to as Base Case, Upper Case, and Lower Case.

Percentile	Case	Year	Bottom Can Temp [K]	Left Drift Temp [K]	Top Drift Temp [K]
50th	Lower	167	346	344	344
	Base	140	341	339	338
	Upper	124	335	333	333
75th	Lower	163	356	353	353
	Base	137	350	347	346
	Upper	120	343	340	339
95th	Lower	140	371	368	367
	Base	128	364	361	360
	Upper	111	355	351	350

FLAC V7.0 (Itasca 2011) was used for 2-D plane-strain simulation of a waste package surrounded by crushed salt, within a rectangular tunnel opening. The built-in *pwipp* and *cwipp* viscoplastic models for intact and crushed salt were used with default values. Three equations to represent temperature dependent thermal conductivity were used to investigate the magnitude of temperature deviation that could be expected.

While the choice of constitutive model to represent the viscoplasticity of salt has little impact peak near field temperatures in a thermo-mechanical study, the hydrology of the system, which is not included in this study, does. Every study into temperature dependent thermal conductivity of salt has noted the release of brines upon heating of the samples. Heat-generating waste in a salt formation would liberate included fluid and result in a multiphase liquid vapor flow which could have significant thermal implications. It is difficult to draw realistic conclusions of the time dependent temperature history with a purely thermo-mechanical analysis. Hydraulic fracturing could occur and if found to have an impact on bulk thermal conductivity, may result in increased repository temperatures. The rate of hydraulic damage would have to exceed the rate that the salt can self-heal. Future analysis would benefit from including hydrology. The creep behavior would also be more accurately predicted by using a more recent viscoplastic model such as Munson-Dawson (Munson et al., 1989).

4. REFERENCES

Banerjee, K., , K.R. Robb, G. Radulescu, J.M. Scaglione, J.C. Wagner, J.B. Clarity, R.A. LeFebvre and J.L. Peterson 2016. "Estimation of Inherent Safety Margins in Loaded Commercial Spent Nuclear Fuel Casks," *Nuclear Technology*. 195:2, p. 124-142.

Bauer, S., Urquhart, A., 2014. Thermophysical Properties of Reconsolidating Crushed Salt. SAND2014-2240. Sandia National Laboratories. Sandia National Laboratories, Albuquerque, NM, USA.

Bauer, S., Urquhart, A., 2015. Thermal and Physical Properties of Reconsolidated Crushed Rock Salt as a Function of Porosity and Temperature. Acta Geotech. Doi.org/10.1007/s11440-015-0414-8.

Bechthold, W., E. Smailos, S. Heusermann, W. Bollingerfehr, B. Bazargan Sabet, T. Rothfuchs, P. Kamlot, J. Grupa, S. Olivella, and F.D. Hansen 2004. *Backfilling and Sealing of Underground Repositories for Radioactive Waste in Salt (BAMBUS II Project), Final Report*. EUR 20621, Nuclear Science and Technology, Luxembourg.

Chang, K.W., Nole, M., Stein, E., 2021. Reduced-order modeling of near- field THMC coupled processes for nuclear waste repositories in shale. Comput. Geotech. 138, 104326. doi:10.1016/j.compgeo.2021.104326.

Chen, D., Pan, Z.J., Ye, Z.H., 2015. Dependence of gas shale fracture permeability on effective stress and reservoir pressure: model match and insights. Fuel 139, 383–392. doi:10.1016/j.fuel.2014.09.018.

Clarity, J., K. Banerjee, H.K. Liljenfeldt and W.J. Marshall 2017 "As-Loaded Criticality Margin Assessment of Dual-Purpose Canisters Using UNF-ST&DARDS." *Nuclear Technology*. 199:3, pp. 245-275.

Dewhurst, D.N., Aplin, A.C., Sarda, J.P., 1999. Influence of clay frac- tion on pore-scale properties and hydraulic conductivity of experimentally compacted mudstones. IJ. Geophys. Res. Solid Earth 104, 29261–29274. doi:10.1029/1999JB900276.

Gonzales, S. and K.S. Johnson, 1985. Shales and Other Argillaceous Strata in the United States. Oak Ridge National Laboratory. Oak Ridge, TN**:** 596.

Ingebritsen, S., Sanford, W., Neuzil, C., 2006. Groundwater in Geologic Processes. Second Edition: Cambridge University Press. 536 pp.

Itasca (Itasca Consulting Group) 2011. *FLAC Version 7.00 User's Guide*. Minneapolis, MN.

Jobmann, M., Buntebarth, G., 2009. Influence of graphite and quartz ad- dition on the thermo-physical properties of bentonite for sealing heat- generating radioactive waste. Appl. Clay Sci. 43, 206–210. doi:10.1016/ j.clay.2009.01.016.

Jones, P., Chang, K.W., Hardin, E., 2021. DPC Disposal Thermal Scoping Analysis. SAND2021-7515R, Sandia National Laboratories, Albuquerque, NM, USA.

Kwon, O., Kronenberg, A.K., Gangi, A.F., Johnson, B., 2001. Permeability of Wilcox shale and its effective pressure law. J. Geophys. Res. Solid Earth 106, 19339–19353. doi:10.1029/2001JB000273.

LaForce, T., Basurto, E., Chang, K.W., Jayne, R.S., Leone, R.C., Nole, M., Perry, F.V., Stein, E., 2021. GDSA Repository Systems Analysis Investigations in FY2021. SAND2021-11691R, Sandia National Laboratories, Albuquerque, NM, USA.

LaForce, T., Chang, K.W., Perry, F.V., Lowry, T.S., Basurto, E., Jayne, R.S., Brooks, D.M., Jordan, S.H., Stein, E.R., Leone, R.C., Nole, M., 2020. GDSA Repository Systems Analysis Investigations in FY2020. SAND2020-12028R, Sandia National Laboratories, Albuquerque, NM, USA.

Lichtner, P.C., Hammond, G.E., 2012. Quick Reference Guide: PFLOTRAN 2.0: Multiphase-Multicomponent-Multiscale Massively Parallel Reactive Transport Code. LA-CC-09-047, Los Alamos National Laboratory, Los Alamos, NM, USA.

Liu, H.H., Rutqvist, J., Berryman, J.G., 2009. On the relationship between stress and elastic strain for porous and fractured rock. Int. J. Rock Mech. Min. Sci. 46, 289–296. doi:10.1016/j.ijrmms.2008.04.005.

Liu, J.F., Song, Y., Skoczylas, F., Liu, J., 2016. Gas migration through water-saturated bentonite-sand mixtures, COx argillite, and their inter- faces. Can. Geotech. J. 53(1), 60–71. doi:10.1139/cgj-2014-0412.

Mariner, P.E., M. A. Nole, M., Basurto, E., Berg, T.M., Chang, K.W., De- busschere, B.J., Eckert, A.C., Ebeida, M.S., Gross, M., Hammond, G.E., Harvey, J., Jordan, S.H., Kuhlman, K.L., LaForce, T.C., Leone, R.C., III, W.C.M., M. M. Mills, M., Park, H.D., Perry, F.V., III, A.S., Seidl, D.T., Sevougian, S.D., Stein, E.R., Swiler, L.P., 2020. Advances in GDSA Framework Development and Process Model Integration. SAND2020- 10787R, Sandia National Laboratories, Albuquerque, NM, USA.

Mariner, P.E., Berg, T.M., Chang, K.W., Debusschere, B.J., Eckert, A.C., Harvey, J., LaForce, T., Leone, R.C., Mills, M.M., Nole, M., Park, H.D., Perry, F.V., Seidl, D.T., Swiler, L.P., 2021. GDSA Framework Develop- ment and Process Model Integration FY2021. SAND2021-12626R, Sandia National Laboratories, Albuquerque, NM, USA.

Mellegard, K., Callahan, G., Hansen, F., 2013. High-temperature characterization of bedded Permian salt. 47th US rock mechanics/geomechanics symposium. SAND2013-4040J.

Munson, D.E., Fossum, A.F., and Senseny, P.E. 1989. Advances in Resolution of Discrepancies between Predicted and Measured WIPP In-situ Room Closures. Sandia National Laboratories, Albuquerque, NM. SAND88-2948.

Munson, D.E., Jones, R.L., Ball, J.R., Clancy, R.M., Hoag, D.L., and Petney, S.V. 1990. Overtest for simulated defense high-level waste (Room B): Insitu data report (May 1984-February 1988). SAND-89-2671. Sandia National Laboratories, Albuquerque, NM, USA.

Paneru, L.P., Bauer, S.J., Stormont, J.C., 2018. Thermal Properties of Consolidated Granular Salt as a Backfill Material. *Rock Mech Rock Eng* 51, 911–923 (2018). https://doi.org/10.1007/s00603-017-1353-5

Rechard, R.P., B. Goldstein, L.H. Brush, J.A. Blink, M. Sutton, and F.V. Perry (2011), Basis for Identification of Disposal Option for Research and Development for Spent Nuclear Fuel and High- Level Waste. FCRD-USED-2011-000071. SAND2011-3781P, Sandia National Laboratories, Albuquerque, New Mexico.

Robinson, E.C. 1988. *Thermal Properties of Rocks*. USGS Open File Report 88-441. U.S. Geological Survey.

Rutqvist, J., Tounsi, K., 2021. Geomechanical and Performance Assessment Impacts of DPC Disposal in Various Host Rock Environments. Prepared for U.S. Department of Energy Spent Fuel and Waste Science and Technology, M4SF-21LB010305041. Lawrence Berkeley National Laboratory.

Rutqvist, J., Y. Ijiri, and H. Yamamoto (2011), Implementation of the Barcelona Basic Model into TOUGH–FLAC for simulations of the geomechanical behavior of unsaturated soils. Comput. Geosci. 37, 751–762.

Sass, J.H., Lachenbruch, A.H., Munroe, R.J., 1971. Thermal conductivity of rocks from measurements on fragments and its application to heat-flow determinations, Journal of Geophysical Research, V. 76, p. 3391–3401.

Senseny, P.E. 1985. "Determination of a Constitutive Law for Salt at Elevated Temperature and Pressure." Measurement of Rock Properties at Elevated Pressures and Temperatures (H.J. Pincus and E.R.

Hoskins, eds.). American Society for Testing and Materials, Special Technical Publication 869. Philadelphia, PA.

Sevougian, S.D., Stein, E.R., LaForce, T., Perry, F., Nole, M., Chang, K.W., 2019. GDSA Repository Systems Analysis FY19 Update. SAND2019- 11942R, Sandia National Laboratories, Albuquerque, NM, USA.

Shelton, S.M., 1934. Thermal conductivity of some irons and steels over the temperature range 100 to 500°C. Bureau of Standards Journal of Research, 12(4/6), 441–450.

Shurr, G.W. (1977), The Pierre Shale, Northern Great Plains: A Potential Isolation Medium for Radioactive Waste. Open-File Report. United States Geological Survey. Reston, VA**:** 27.

Smith, D., 1976. Thermal Conductivity of Halite Using a Pulsed Laser. Report No.:Y/DA-7013. Oak Ridge Y-Plant; 1976. Contract No.:W-7405-eng-26. Oak Ridge, Tennessee, USA.

Somerton, W., Keese, J., Chu, S., 1974. Thermal behavior of unconsolidated oil sands. J. Soc. Petrol. Engr. 14, 513–521.

Wang, M., Chen, Y.F., Zhou, S., Hu, R., Zhou, C.B., 2015. A homogenization-based model for the effective thermal conductivity of bentonite-sand-based buffer material. Int. Commun. Heat Mass Transf. 68, 43-49. Doi:10.1016/j.icheatmasstransfer.2015.08.007.

Zheng, J., Zheng, L., Liu, H.H., Ju, Y., 2015. Relationships between permeability, porosity and effective stress for low-permeability sedimentary rock. Int. J. Rock Mech. Min. Sci. 78, 304–318. doi:10.1016/j.ijrmms.2015.04.025.